Developing a Robust Recombination Contact to Realize Monolithic Perovskite Tandems With Industrially Common p-Type Silicon Solar Cells

Robert L. Z. Hoye [ORCID], Kevin A. Bush, Felipe Oviedo, Sarah E. Sofia [ORCID], Maung Thway [ORCID], Xinhang Li, Zhe Liu [ORCID], Joel Jean [ORCID], Jonathan P. Mailoa, Anna Osherov, Fen Lin, Axel F. Palmstrom, Vladimir Bulović, Michael D. McGehee, Ian Marius Peters [ORCID], and Tonio Buonassisi

Abstract—**Although two-terminal perovskite-silicon tandem solar cells have rapidly increased in efficiency, they have only been demonstrated with n-type silicon, which currently constitutes less than 5% of the global photovoltaics market. In this paper, we realize the first two-terminal perovskite tandem with p-type silicon by developing a recombination contact that enables voltage addition without damaging either subcell. We find that silicon interband recombination contacts are limited by a SiO_x charge-extraction barrier, which forms during oxidative top-cell fabrication. A sputtered 30-nm indium tin oxide layer is found to protect the silicon cell surface from oxidation, while forming a recombination contact with the p-type nickel oxide hole transport layer for the perovskite top cell. Using this recombination contact we achieve voltage addition between the perovskite top cell and aluminum back-surface field p-type silicon bottom cell. We also find that minimizing moisture on the nickel oxide surface is important for achieving a stable open-circuit voltage under illumination. The recombination contact developed herein could play an important role in near-future developments.**

Index Terms—**Aluminum back-surface field (Al-BSF), nickel oxide, perovskite-silicon tandem solar cells, p-type silicon cell, recombination contact, stability.**

I. INTRODUCTION

SINGLE junction photovoltaics (PVs) based on organic–inorganic hybrid lead halide perovskites have rapidly increased in efficiency from 3.8% in 2009 to a certified 22.1% in 2016 [1], [2]. While methylammonium lead iodide ($MAPbI_3$) is unstable in humid air [3], recent efforts have identified perovskite compositions that are more environmentally stable [4], and device architectures that lead to less degradation [5], [6]. With a high absorption coefficient, long diffusion length, and a bandgap that is tunable from 1.55 to 2.3 eV through the halide content [7], [8], these new perovskite compositions have emerged as promising top-cell absorbers for tandems with silicon [9].

Crystalline silicon solar cells currently dominate the PVs market, accounting for over 90% of global production capacity [10]. To achieve and maintain cost-competitiveness with incumbent electric generation sources, however, PV system costs must continue to decline [11], [12]. Increasing the efficiency of silicon solar cells through tandems with perovskite top cells by low-capital-intensity solution processing is an appealing option [13]. In these tandems, the wider bandgap perovskite top cell absorbs the visible light, converting energy that would otherwise be lost through thermalization in the 1.1 eV bandgap silicon bottom cell. The addition of a wide-bandgap top cell increases the radiative efficiency limit from 32.9% to 45% [14].

The four-terminal and two-terminal configurations are two of the most commonly used architectures for tandems. The four-terminal approach involves mechanically stacking individually fabricated single-junction devices [9], [15]. Such four-terminal tandems were realized in 2014 with an efficiency of 17% [16], increasing to 26% in 2017 [17].

By contrast, the two-terminal (or monolithic) tandem architecture has the perovskite top cell directly grown on the silicon bottom cell [5]. Monolithic tandems can achieve lower manufacturing costs, are simpler to incorporate into modules, and can reach higher efficiencies than four-terminal tandems due to lower optical and resistance losses by avoiding the need for additional transparent electrodes and metal grids [9], [18], [19]. The two-terminal architecture is, however, more challenging to implement, requiring current matching and the compatibility of the processing of the top cell with the silicon bottom cell [18]. The first two-terminal perovskite-silicon tandem was reported by Mailoa et al. in 2015, demonstrating a stabilized efficiency of 13.7% with an n-type silicon bottom cell [13]. This device used a silicon interband recombination contact, comprised of p^{++} and n^{++} silicon. Albrecht et al. then Werner et al. reported improved monolithic tandems on n-type silicon heterojunction cells with efficiencies of 18% and 21.2%, respectively [20], [21]. We subsequently improved the efficiency to a certified 23.6% with 1000 h stability under dry and damp environments using a protective atomic-layer-deposited (ALD) tin oxide and sputtered indium tin oxide (ITO) top electrode [5].

Although the development of monolithic tandems has focused on n-type silicon bottom cells, it is technologically and commercially important to develop architectures that enable efficient integration of perovskites with the more industrially common p-type silicon cells. p-type silicon accounts for over 85% of the current global PVs market [10]. Another advantage of p-type silicon cells is that there is a wider temperature processing window for the charge transport layers deposited on top (up to 500 °C [13]), whereas silicon heterojunction cells can only be processed below 250 °C to avoid damaging the amorphous passivation layers. Realizing monolithic tandems with p-type silicon requires developing a recombination contact with inverted polarity compared with the previous work on n-type silicon. The recombination contact needs to be both optically transparent to near-infrared light and sufficiently robust to protect the silicon bottom cell during processing of the top cell.

In this paper, we systematically developed each component of the recombination contact to realize monolithic perovskite tandems on p-type aluminum back-surface field (Al-BSF) silicon bottom cells made with industry-standard process flows. We investigated silicon interband recombination contacts, but found them to be susceptible to the formation of a current-limiting SiO$_x$ barrier during top-cell synthesis. Using X-ray photoemission spectroscopy (XPS), we found the SiO$_x$ to form not only during UV-ozone or oxygen-plasma treatment, but also during the deposition and annealing of the NiO$_x$ layer on top. We overcame this limitation by replacing the silicon interband recombination contact with ITO sputtered without oxygen working gas, and forming a recombination contact with NiO$_x$. As a result, we realized a 1 cm^2 area tandem that achieved voltage addition. We also found that minimizing moisture accumulation on the surface of NiO$_x$ enabled the open-circuit voltage (V_{OC}) to be stable under illumination. The architecture developed here could play an important role in the commercial integration of low-capital-intensity perovskites with the dominant material in the PVs industry today.

II. METHODS

A. Fabrication of Single-Junction Perovskite Devices

ITO/glass substrates (Thin-Film Devices) were cleaned in acetone and isopropanol by ultrasonication for 15 min successively. The substrates were blown dry with nitrogen gas and oxygen-plasma-cleaned for 10 min, following a previous report [3]. PEDOT:PSS (Ossila) was deposited onto ITO/glass by spin-casting at 4000 r/min for 30 s, followed by annealing at 130 °C in air for 20 min. NiO$_x$ was deposited by preparing a solution of 1 mol L^{-1} nickel nitrate hexahydrate (99.999%, Sigma-Aldrich) and ethylenediamine ($\geq$99%, Sigma-Aldrich) in ethylene glycol (99.8%, Sigma-Aldrich), which was filtered with a 0.2 μm pore PTFE filter. The solution was spread over the substrate and spun at 2000 r/min for 90 s. These films were annealed at 100 °C for 30 min, followed by 300 °C for 1 h in air or inside a dry box with a relative humidity <10%. The NiO$_x$ was oxygen plasma treated for 5 min. The methylammonium lead iodide (MAPbI$_3$) precursor solution was prepared by dissolving 166.7 mg lead acetate trihydrate (99.999%, Sigma-Aldrich) and 212 mg methylammonium iodide (Dyesol) in 0.5 mL N, N–dimethylformamide (99.8%, Sigma-Aldrich). The solution was stirred for 15 min at 50 °C. The perovskite was deposited inside the dry box. The perovskite solution was pre-heated to 50 °C and substrates to 85 °C before dynamically depositing 35 μL solution onto the 12 × 12 mm^2 substrate spinning at 2200 r/min. The substrate was spun for a total of 90 s before immediately annealing the film at 85 °C for 20 min. The perovskite was stored in the dry box for 4 h before transferring to a nitrogen-filled glovebox. 35 mg mL^{-1} PC$_{60}$BM (nano-C) dissolved in chlorobenzene (99.8%, Sigma-Aldrich) was deposited dynamically onto the perovskite spinning at 1400 r/min for 40 s, then 3000 r/min for 10 s. 20 nm Ca and 80 nm Al were thermally evaporated through a shadow mask at 10^{-6} Torr pressure to create an active area of 5.44 mm^2 for each device.

B. Fabrication of Silicon Cells

For Al-BSF cells, p^{++} silicon cells (Silicon Quest) were rear-textured from the wafer diamond sawing process and had an Au rear-electrode evaporated. The rear-textured p-type silicon bottom cells were prepared by diffusing a doped n^{++} emitter into the front surface of the silicon using standard POCl$_3$ diffusion at 865 °C for 10 min. The back surface of the cell was subsequently metallized by sputtering 1 μm Al. The sample was annealed at 900 °C for 30 s to achieve back-surface field passivation. The silicon interband recombination contact was made by depositing a 2–3 nm thick layer of intrinsic amorphous silicon, followed by 30 nm of heavily doped p-type hydrogenated amorphous silicon by plasma-enhanced chemical vapor deposition (PECVD) at 250 °C on the front surface of the silicon wafer. The samples subsequently underwent a rapid thermal anneal at 680 °C for 900 s to recrystallize the amorphous silicon. UV-ozone treatment was performed using a UVOCS Inc. system for 5 min. Oxygen plasma treatment was performed following a previous report [3]. Silicon single-junction devices were made by depositing 70 nm SiN$_x$ onto the silicon bottom cells by PECVD, followed by a metal grid comprised of 20 nm Ti, 20 nm Pd, and 250 nm Ag using e-beam evaporation. The devices were cleaned in solvents,

annealed at 400 °C for 300 s to improve metal adhesion, then laser scribed to form 1×1 cm^2 devices.

C. Fabrication of Tandems With 1 cm^2 Active Area

The p-type silicon cells described in Section II-B were cut to 14×14 mm^2 substrates, and mesa etched so that the emitter covered an 11×11 mm^2 area. The surface SiO$_x$ layer on the silicon cells was removed by etching with 10% HF. About 30 nm ITO was deposited by RF magnetron sputtering over a 12×12 mm^2 area at a rate of 0.6–0.7 Å s^{-1} with an Ar partial pressure of 6 mTorr and RF power of 60 W (1.3 W cm^{-2}). An ITO target (99.99% purity, 90% In$_2$O$_3$, 10% SnO$_2$ by mass, Plasmaterials) was used. No substrate heating was employed. NiO$_x$ was synthesized in a similar way as Section II-A, but spun at 5000 r/min for 45 s to give an 8 nm thick film. Cs$_{0.17}$FA$_{0.83}$Pb(Br$_{0.17}$I$_{0.83}$)$_3$ was deposited according to a previously reported method [5]. The precursor solution contained CsI (99.99%, Sigma-Aldrich), FAI (Dyesol), PbI$_2$ (TCI), PbBr$_2$ (96%, Sigma-Aldrich), and the solvents N, N-diemthylformamide (99.8%, Sigma Aldrich) and dimethyl sulfoxide ($\geq$99.9%, Sigma-Aldrich). The solution was spun in a dry air box at 1000 r/min for 11 s, followed by 6000 r/min for 30 s, with chlorobenzene dropped 5 s from the end. The films were annealed at 50 °C for 10 s, then 100 °C for 30 min. 1 nm LiF and 20 nm C_{60} (>99.9%, MER Corporation) were thermally evaporated, followed by ALD of 4 nm SnO$_2$ and 2 nm zinc tin oxide at 100 °C in an Arradiance GEMStar-6 system. The tin precursor was tetrakis(dimethylamido)tin (TDMASn), zinc precursor diethylzinc (DEZ), and oxidant vapors of deionized water. Each SnO$_2$ cycle comprised of 1.5 s TDMASn pulse, 5 s purging with 90 mL min^{-1} N$_2$, 1 s H$_2$O pulse, 5 s purging. The TDMASn precursor was heated to 60 °C. Zinc tin oxide was grown using a supercycle comprised of three cycles of SnO$_2$ and three cycles of Zno. Each ZnO cycle had 100 ms DEZ pulse, 5 s purge, 1 s H$_2$O pulse, 5 s purge. ITO and LiF (as an antireflection coating) were sputtered and evaporated respectively according to a previous report [5].

D. Characterization

Transmittance measurements were performed inside an integrating sphere using a PerkinElmer Lambda 950 UV-VIS-NIR spectrophotometer. The transmittance of the glass substrate was also measured and divided from the measured transmittance of the thin film on glass, to account for the reflectance and absorptance of the glass substrate. Solar simulations were performed under 1 sun AM 1.5G illumination, calibrated with a silicon reference cell using a Newport solar simulator inside a nitrogen-filled glovebox for the single-junction devices, Newport solar simulator in air for the perovskite devices on silicon, and Oriel Sol3A solar simulator for the 1 cm^2 area tandems. The measured performance was not adjusted for the spectral mismatch of the subcells. For the single-junction devices, the active area was apertured to 1 mm^2. For the devices on p-type silicon, the 5.44 mm^2 devices were apertured to 3.36 mm^2 for current-density versus voltage (J–V) measurements. For the 1 cm^2 area tandems, the devices were apertured to 1 cm^2. The devices were not apertured for open-circuit voltage measurements. The current–voltage sweeps and open-circuit voltage measurements
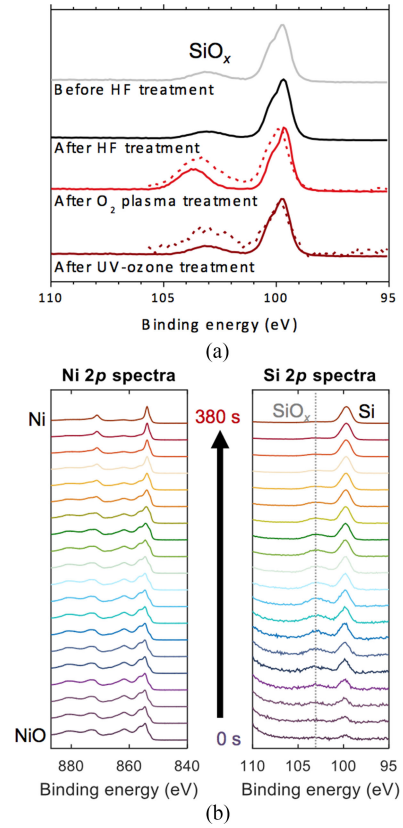

Fig. 1. X-ray photoemission spectroscopy (XPS) investigation of silicon interband recombination contacts. (a) Si 2p spectra of silicon bottom cells, showing increased SiO$_x$ signal after NiO$_x$ deposition and annealing (dashed lines). (b) XPS depth-profile measurements for NiO$_x$ on UV-ozone-treated silicon, with the sputtering time labeled, and the SiO$_x$ peak position indicated by a gray line. Time = 0 s corresponds to the surface of the NiO$_x$. Time = 380 s corresponds to bulk silicon after sputtering through the NiO$_x$ and SiO$_x$ layers.

were obtained with a Keithley 2400 digital sourcemeter. EQE measurements were performed according to a previous report [5]. The XPS spectra were collected using a Thermo Scientific K-Alpha XPS. Monochromatic Al K_α X-rays (1486.6 eV excitation energy) were used as the source and the measurements performed under 8×10^{-8} mbar base pressure with a photoelectron take-off angle of 90°. The spectral positions were corrected by adjusting to the C 1 s adventitious peak at 284.80 eV. Depth profiling was obtained by gentle sputtering of the sample with an Ar cluster source (2000 atoms per cluster) at 6 keV for 10 s, followed by spectral collection. We note that in Fig. 1(b), only every second spectrum is shown for clarity (i.e., the spectra are separated by 20 s intervals). The thicknesses of the NiO$_x$, MAPbI$_3$, and PEDOT:PSS films were measured by variable-angle spectroscopic ellipsometry using a rotating-analyzer ellipsometer (J.A. Woollam VASE). Ellipsometry data from 280–2500 nm were obtained at incident angles of 65°, 70°, and 75° and fitted with generalized oscillator models using WVASE32 software (Woollam). The sheet resistance of ITO was measured using a 4-point probe from Jandel Engineering. A Keithley 2400 source meter was used to sweep from −30 to 30 mV and measure the current. Using the resistance from the Ohmic current–voltage curve measured and the standard $\pi/\ln(2)$ correction factor for in-line probes, the sheet resistance was calculated.

III. RESULTS AND DISCUSSION

A. Challenges of Silicon Interband Recombination Contacts for Monolithic Tandems with p-Type Silicon

We first investigated the use of a silicon interband recombination contact with opposite polarity to that previously used for n-type silicon. This recombination contact (comprised of n^{++} and p^{++} silicon) is advantageous because it has minimal optical absorption [13]. However, our first attempts resulted in extraction barriers (see Fig. S1, Supporting Information). To identify the root cause, we characterized the silicon bottom cell by XPS and found that a thicker layer of insulating SiO_x formed on the silicon surface [see Fig. 1(a)] after the oxygen-plasma treatment needed for sufficient wetting of the solution-processed top cell. We investigated whether this effect could be overcome by using 5 min UV-ozone treatment instead to make the silicon hydrophilic. We found that while the SiO_x peak was smaller [see Fig. 1(a)], the tandems still had extraction barriers (see Fig. S1, Supporting Information).

For our solution-processed top cell, we considered using PEDOT:PSS or nickel oxide (NiO_x) as the hole transport layer. Both were effective hole acceptors and did not change the perovskite phase (see Section S2, Supporting Information), but our 20 nm NiO_x films were more suitable because they had higher near-infrared transmittance (>95%) and gave higher open-circuit voltage in our test single-junction $MAPbI_3$ perovskite top cells (1.07 ± 0.02 V cf., 0.906 ± 0.004 V), leading to higher efficiencies (see Table S2, Supporting Information). However, our solution-processed NiO_x layer required crystallization for 1 h in air at 300 °C. To investigate whether this led to further damage of our silicon interband recombination contact, we performed XPS depth-profiling through the NiO_x film. In Fig. 1(b), it can be seen that the Si 2p spectra were initially almost featureless because most of the photoelectrons were collected from the NiO_x surface. During sputtering, the Ni 2p spectra changed from Ni^{2+} to an elemental Ni doublet as the Ni–O bonds were broken, while the Si 2p peaks became more intense until only the peak corresponding to elemental silicon at 99 eV binding energy was observed [see Fig. 1(b)]. These spectra after 380 s sputtering correspond to when both the NiO_x and SiO_x layers have been removed, with some Ni implanted into silicon during the sputtering process. We were therefore able to obtain the XPS spectrum of the SiO_x layer under NiO_x in the middle of the depth-profile. This SiO_x peak after NiO_x annealing is larger than that for silicon after UV-ozone treatment [see Fig. 1(a)] showing that a thicker SiO_x formed after crystallizing our NiO_x layer. This may be due to either oxygen diffusing through the 20 nm NiO_x layer or an increased rate of silicon oxidation when Si–Ni bonds form, as has been observed in nickel silicides [22]. These results suggest that silicon interband layers are damaged during the processing of our solution-synthesized top cell and not suitable as recombination contacts.

B. Overcoming Bottom Cell Oxidation Using an ITO/NiOx Recombination Contact

We investigated whether depositing ITO on silicon before depositing NiO_x could protect the bottom cell from oxidation during processing. We 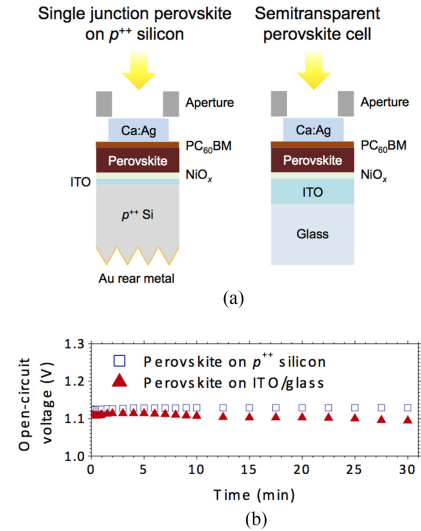believed it was possible to deposit a conductive ITO layer on silicon without oxidizing it because this is a part of the standard process for fabricating silicon heterojunction solar cells [18]. Degenerate n-type doping in ITO is primarily caused by oxygen vacancies, supplemented by substitutional tin doping [23], [24]. As a result, ITO films sputtered without oxygen working gas can achieve low resistivity and high transparency, although a low concentration of O_2 may help maintain film stoichiometry and high optical transmission [23], [25].

To determine whether sputtering ITO led to silicon oxidation, we compared single-junction perovskite devices on ITO-coated p^{++} silicon, and on standard ITO/glass [device structures in Fig. 2(a)]. Both were illuminated through a Ca:Ag transparent top electrode to enable a fair comparison between the devices on opaque p^{++} silicon and on transparent glass substrates. Ca:Ag was chosen because it could be evaporated at a low rate of 0.4 Å s^{-1}, preventing damage to the $PC_{60}BM$ layer. Both types of devices were expected to operate similarly if no oxidation occurred because the p^{++} silicon is degenerate like ITO. The p^{++} silicon was contacted from the rear gold electrode. If oxidation occurred on the p^{++}-silicon-based device, we would have expected an extraction barrier. This extraction barrier was absent and the two types of devices had very similar performance (see Fig. S2, Supporting Information), suggesting that the ITO can protect the silicon from oxidation during top-cell processing.

C. Controlling the Open-Circuit Voltage Stability of the Perovskite Top Cell

We found that maintaining a stable open-circuit voltage under illumination required careful control of the surface properties of the NiO_x layer. When NiO_x was annealed and left in air for 2.5 h, the open-circuit voltage decreased by 25 meV after 30 min illumination under 1 sun [see Fig. S6(a), Supporting Information, olive points]. In contrast, when NiO_x was annealed inside a dry box with <10% relative humidity, the open-circuit voltage after 30 min was almost the same as the initial value.

Fig. 2. (a) Device structure and (b) open-circuit voltage versus time of perovskite single-junction devices on ITO/ p^{++} silicon and ITO/glass. Both devices were measured in air.

This article has been accepted for inclusion in a future issue of this journal. Content is final as presented, with the exception of pagination.

HOYE *et al.*: DEVELOPING A ROBUST RECOMBINATION CONTACT TO REALIZE MONOLITHIC PEROVSKITE TANDEMS 5

To understand these effects, we investigated the following three hypotheses:

1) perovskite damage due to the formation of surface hydroxyl groups when NiO_x is kept in humid air;
2) perovskite deprotonation over time due to the high isoelectric point of NiO_x;
3) perovskite change due to moisture accumulation at the interface between NiO_x and $MAPbI_3$.

As detailed in Section S2 of the Supporting Information, we found the third hypothesis to be the most likely. Fourier transform infrared spectroscopy measurements showed that moisture accumulated on the NiO_x over time in ambient air. When the NiO_x was taken into the dry box immediately after annealing, there was no decrease in the open-circuit voltage [see Fig. S6(a), Supporting Information, red points]. Similarly, when NiO_x left in air for 2.5 h was subsequently heated to drive off moisture, there was also no decrease in open-circuit voltage [see Fig. S6(a), Supporting Information, open circles]. The open-circuit voltage of our $MAPbI_3$ devices may degrade when moisture is present due to the reversible formation of a layered hydrated phase, which can lead to nonradiative recombination [26]. The high potential under open-circuit conditions may favor the formation of hydrated $MAPbI_3$ if a greater quantity of moisture accumulates on the surface of the HTL. Our results (discussed in detail in Section S2, Supporting Information) indicate that while a NiO_x HTL gives a higher open-circuit voltage than PEDOT:PSS, to maintain a stable open-circuit voltage, it is important to minimize the exposure of the NiO_x surface to moisture after annealing. This information is important not only for the present work on tandems, but also for achieving greater reproducibility in perovskite devices using NiO_x. Using these processing conditions, we achieved perovskite devices on p^{++} silicon with an open-circuit voltage that was stable under constant 1 sun illumination for the duration of the 30 min experiment [see Fig. 2(b)].

D. 1 cm² Active Area Monolithic Perovskite Tandems With p-type Silicon Solar Cells

To determine whether our ITO/NiO_x recombination contact can enable voltage addition, we fabricated monolithic tandems with p-type Al-BSF silicon cells. The tandem device structure is shown in Fig. 3(a), and the band diagram of the ITO/NiO_x recombination contact is given in Fig. 3(b). To minimize losses due to dark current from the silicon bottom cell, the perovskite top-cell active area is required to match that of the silicon subcell (1 cm²). We therefore used a perovskite top cell we previously optimized for 1 cm² active areas [5]. This cell consisted of $Cs_{0.17}FA_{0.83}Pb(Br_{0.17}I_{0.83})_3$ perovskite, where FA is formamidinium, with electron transport layers deposited by thermal evaporation and ALD to avoid pinholes (details in Section II). The ALD SnO_2 and zinc tin oxide layers protected the $PC_{60}BM$ and perovskite from damage when sputtering the 150-nm top transparent ITO electrode, which had a low sheet resistance of 30 $\Omega/\square$. A labeled cross-sectional SEM image of the monolithic tandem is shown in Fig. 3(c).

The J–V curve for the tandem showed almost no hysteresis [see Fig. 3(d)], and the short-circuit current density, open-circuit voltage, and maximum power point matched the stabilized values (black diamonds). The V_{OC} of the tandem was 1.43 V, suc-
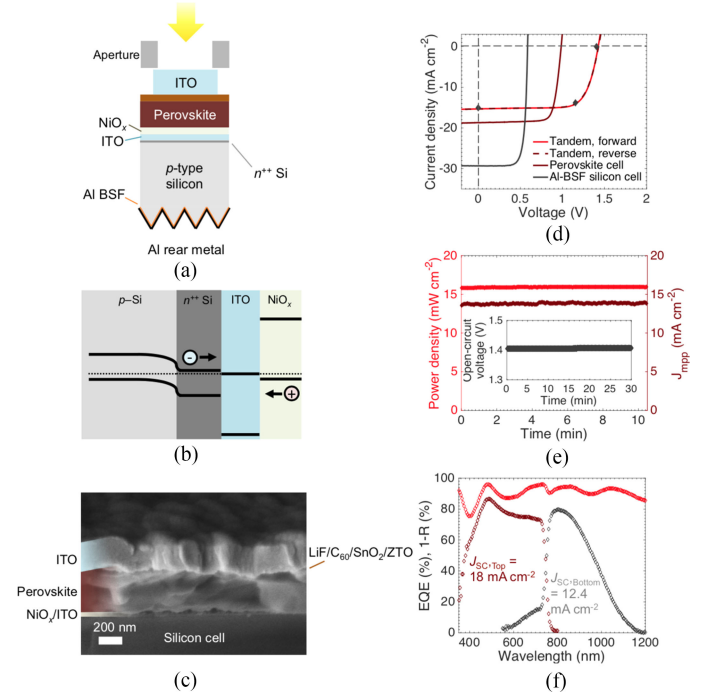

Fig. 3. Monolithic tandems with an active area of 1 cm² using ITO/NiO_x recombination contacts measured under 1 sun AM 1.5G illumination. (a) Device structure of tandems with Al-BSF p-type silicon bottom cells. (b) Band structure of the ITO/NiO_x recombination contact on a p-type silicon cell. (c) Cross-sectional scanning electron microscopy image of a tandem on silicon. We note that the $LiF/C_{60}/SnO_2/ZTO$ layers are between the perovskite and ITO, and are too thin to resolve. (d) J–V curve swept at 100 mV s⁻¹ in both the forward (solid line) and reverse (dashed line) directions for the tandem device. The stabilized short-circuit current density, maximum power point, and open-circuit voltage are shown as black diamonds. The J–V curve for a semitransparent $Cs_{0.17}FA_{0.83}Pb(Br_{0.17}I_{0.83})_3$ perovskite cell and unfiltered silicon single-junction device made from the same p-type silicon wafer as the bottom cell are also shown. (e) Power and current density at the maximum power point, and open-circuit voltage versus time (inset) over a period of 30 min. (f) Tandem 1-R (reflectance) and external quantum efficiency of the top and bottom subcells.

TABLE I
PERFORMANCE OF SINGLE JUNCTION AND TANDEM SOLAR CELLS UNDER 1-SUN ILLUMINATION (WITHOUT SPECTRAL MISMATCH CORRECTION)

Cell type	V_{OC} (V)	FF (%)	PCE (%)	J_{SC} (mA cm⁻²)	
				From J–V	From EQE
Perovskite top cell	0.98	79	14.5	18.7	17.9
Silicon bottom cell (unfiltered)	0.58	78	13.3	29.3	33.0
Tandem	1.43	75	16.2	15.3	12.4

The area of the tandem was 1 cm² and measured with a matching aperture area.

cessfully demonstrating voltage addition from the subcells [see Fig. 3(d)]. The tandem efficiency (16.2% from forward and reverse J–V sweeps) matched the stabilized power output [16%, see Fig. 3(e) and Table I], and also exceeded the efficiencies of the subcells (13.3% for the Al-BSF cell, 14.5% for the semitransparent perovskite top cell [Refer to Table I]). Notably, by minimizing the exposure of the NiO_x layer to humid air before depositing the perovskite layer, the tandem V_{OC} remained constant over the entire 30 min testing period [see Fig. 3(e)]. Our tandem results demonstrate the success of the recombination contact and processing strategies we have developed for p-type silicon tandems.

This article has been accepted for inclusion in a future issue of this journal. Content is final as presented, with the exception of pagination.

6   IEEE JOURNAL OF PHOTOVOLTAICS

To identify routes to build off our work and achieve higher efficiencies, we analyzed the losses in our devices. From light-biased external quantum efficiency (EQE) measurements of each subcell, we found that the integrated J_{SC} of the silicon bottom cell (12.4 mA cm^{-2}) was lower than that of the perovskite top cell and also below the J_{SC} of the tandem measured from J–V curves (15.3 mA cm^{-2}). Previous analysis of tandem solar cells has shown that if the current-limiting sub-cell is shunted, then the tandem current density can transition to that of the noncurrent-limiting subcell [27]. Shunting in the silicon bottom cell may also contribute to the 0.13 V difference between the sum of the V_{OC} of each subcell and the V_{OC} of the tandem. The performance of our tandems is also limited by parasitic losses, particularly in the near-infrared spectral range, in which the EQE of the silicon subcell is significantly below 1-R for the tandem [see Fig. 3(f)]. To understand the factors contributing to the large near-infrared parasitic loss, we calculated the EQE of the silicon bottom cell from the measured EQE of the single-junction device and transmittance of the perovskite top cell. The calculated EQE very closely matched the measured EQE, with a similar integrated J_{SC} (see Fig. S8, Supporting Information). We then set the sub-bandgap transmittance of the perovskite to 100% and found that the integrated J_{SC} did not reach that of the perovskite top cell. This shows that the near-infrared response of the silicon cell itself would need to be improved, such as through improved surface passivation or through the use of rear-reflectors covering the textured back surface [5].

IV. CONCLUSION

In summary, we have successfully developed a recombination contact that enables voltage addition between perovskite and p-type silicon subcells in a two-terminal tandem. This was achieved by developing a recombination contact robust to oxidizing top-cell processing, using a sputtered ITO layer to protect the silicon bottom cell. We paired the ITO with an NiO$_x$ hole transport layer, which gave high open-circuit voltages and >95% transmittance for near-infrared light. Control of the moisture content on the surface of NiO$_x$ led to stable open-circuit voltages and stable voltage addition in tandem devices. The advances in tandem architecture and processing developed here could pave the way for the commercialization of perovskites with industry-standard p-type silicon cells as efficient monolithic tandems.

REFERENCES

[1] A. Kojima, K. Teshima, Y. Shirai, and T. Miyasaka, "Organo metal halide perovskites as visible-light sensitizer for photovoltaic cells," *J. Amer. Chem. Soc.*, vol. 131, pp. 6050–6051, 2009.

[2] W. S. Yang *et al.*, "Iodide management in formamidinium-lead-halide–based perovskite layers for efficient solar cells," *Science*, vol. 356, no. 6345, pp. 1376–1379, 2017.

[3] R. Hoye *et al.*, "Methylammonium bismuth iodide as a lead-free, stable hybrid organic-inorganic solar absorber," *Chem. Eur. J.*, vol. 22, no. 8, pp. 2605–2610, 2015.

[4] M. Saliba *et al.*, "Cesium-containing triple cation perovskite solar cells: Improved stability, reproducibility and high efficiency," *Energy Environ. Sci.*, vol. 9, pp. 1989–1997, 2016.

[5] K. A. Bush *et al.*, "23.6%-efficient monolithic perovskite/silicon tandem solar cells with improved stability," *Nature Energy*, vol. 2, no. 4, 2017, Art. no. 17009.

[6] G. Grancini *et al.*, "One-Year stable perovskite solar cells by 2D/3D interface engineering," *Nature Commun.*, vol. 8, 2017, Art. no. 15684.

[7] J. H. Noh, S. H. Im, J. H. Heo, T. N. Mandal, and S. Il Seok, "Chemical management for colorful, efficient, and stable inorganic-organic hybrid nanostructured solar cells," *Nano Lett.*, vol. 13, no. 4, pp. 1764–1769, 2013.

[8] G. E. Eperon *et al.*, "Perovskite-perovskite tandem photovoltaics with optimized band gaps," *Science*, vol. 354, no. 6314, pp. 861–865, 2016.

[9] C. D. Bailie and M. D. McGehee, "High-efficiency tandem perovskite solar cells," *MRS Bull.*, vol. 40, pp. 681–686, 2015.

[10] "International Technology Roadmap for Photovoltaic (ITRPV): 2015 Results,"7th Ed., Mar. 2016. [Online]. Available: http://www.itrpv.net/ Reports/Downloads/2016/, Accessed on: Apr. 10, 2018.

[11] D. B. Needleman *et al.*, "Economically sustainable scaling of photovoltaics to meet climate targets," *Energy Environ. Sci.*, vol. 9, pp. 2122–2129, 2016.

[12] J. Jean, P. R. Brown, R. L. Jaffe, T. Buonassisi, and V. Bulovic, "Pathways for solar photovoltaics," *Energy Environ. Sci.*, vol. 8, no. 4, pp. 1200–1219, 2015.

[13] J. P. Mailoa *et al.*, "A 2-terminal perovskite/silicon multijunction solar cell enabled by a silicon tunnel junction," *Appl. Phys. Lett.*, vol. 106, no. 12, 2015, Art. no. 121105.

[14] T. Todorov, O. Gunawan, and S. Guha, "A road towards 25% efficiency and beyond: perovskite tandem solar cells," *Mol. Syst. Des. Eng.*, vol. 1, pp. 370–376, 2016.

[15] B. Chen *et al.*, "Efficient semitransparent perovskite solar cells for 23.0%-efficiency perovskite/silicon four-terminal tandem cells," *Adv. Energy Mater.*, vol. 6, 2016, Art. no. 1601128.

[16] C. D. Bailie *et al.*, "Semi-transparent perovskite solar cells for tandems with silicon and CIGS," *Energy Environ. Sci.*, vol. 8, pp. 956–963, 2014.

[17] T. Duong *et al.*, "Rubidium multication perovskite with optimized bandgap for perovskite-silicon tandem with over 26% efficiency," *Adv. Energy Mater.*, vol. 7, no. 14, 2017, Art. no. 1700228.

[18] J. Werner *et al.*, "Efficient near-infrared-transparent perovskite solar cells enabling direct comparison of 4-terminal and monolithic perovskite/silicon tandem cells," *ACS Energy Lett.*, vol. 1, pp. 474–480, 2016.

[19] S. E. Sofia, N. Sahraei, J. P. Mailoa, T. Buonassisi, and I. M. Peters, "Metal grid contact design for four-terminal tandem solar cells," *IEEE J. Photovolt.*, vol. 7, no. 3, pp. 934–940, May 2017.

[20] S. Albrecht *et al.*, "Monolithic perovskite/silicon-heterojunction tandem solar cells processed at low temperature," *Energy Environ. Sci.*, vol. 9, pp. 81–88, 2016.

[21] J. Werner *et al.*, "Efficient monolithic perovskite/silicon tandem solar cell with cell area >1 cm^2," *J. Phys. Chem. Lett.*, vol. 7, no. 1, pp. 161–166, 2016.

[22] W. Chen *et al.*, "Efficient and stable large-area perovskite solar cells with inorganic charge extraction layers," *Science*, vol. 350, no. 6263, pp. 944–948, 2015.

[23] S. B. Lee, C. Pincenti, A. Cocco, and D. L. Naylor, "Electronic and optical properties of room temperature sputter deposited indium tin oxide," *J. Vac. Sci. Technol. A*, vol. 11, no. 5, pp. 2742–2746, 1993.

[24] R. B. H. Tahar, T. Ban, Y. Ohya, and Y. Takahashi, "Tin doped indium oxide thin films: Electrical properties," *J. Appl. Phys.*, vol. 83, no. 5, pp. 2631–2645, 1998.

[25] O. Tuna, Y. Selamet, G. Aygun, and L. Ozyuzer, "High quality ITO thin films grown by dc and RF sputtering without oxygen," *J. Phys. D Appl. Phys.*, vol. 43, no. 5, 2010, Art. no. 055402.

[26] A. M. A. Leguy *et al.*, "Reversible hydration of CH 3 NH 3 PbI 3 in films, single crystals, and solar cells," *Chem. Mater.*, vol. 27, no. 9, pp. 3397–3407, 2015.

[27] F. Oviedo, Z. Liu, Z. Ren, M. Thway, T. Buonassisi, and I. M. Peters, "Ohmic shunts in two-terminal dual-junction solar cells with current mismatch," *Jpn. J. Appl. Phys.*, vol. 56, 2017, Art. no. 08MA05.

Authors' photographs and biographies not available at the time of publication.